



Published in final edited form as:

Mol Imaging Biol. 2020 April ; 22(2): 324–334. doi:10.1007/s11307-019-01397-4.

Transcranial Photoacoustic Detection of Blood-Brain Barrier Disruption Following Focused Ultrasound-Mediated Nanoparticle Delivery

Johann Le Floch¹, Hoang D. Lu², Tristan L. Lim², Christine Démoré¹, Robert K. Prud'homme², Kullervo Hynynen¹, F. Stuart Foster¹

¹Department of Medical Biophysics, Sunnybrook Research Institute, 2075 Bayview Avenue, Toronto, ON, M4N 3M5, Canada

²Department of Chemical and Biological Engineering, Princeton University, 50-70 Olden St, Princeton, NJ, 08540, USA

Abstract

Purpose—Blood-brain barrier disruption (BBBD) is of interest for treating neurodegenerative diseases and tumors by enhancing drug delivery. Focused ultrasound (FUS) is a powerful method to alleviate BBB challenges; however, the detection of BBB opening by non-invasive methods remains limited. The purpose of this work is to demonstrate that 3D transcranial color Doppler (3DCD) and photoacoustic imaging (PAI) combined with custom-made nanoparticle (NP)-mediated FUS delivery can detect BBBD in mice.

Procedures—We use MRI and stereotactic ultrasound-mediated BBBD to create and confirm four openings in the left hemisphere and inject intravenously indocyanine green (ICG) and three sizes (40 nm, 100 nm, and 240 nm in diameter) of fluorophore-labeled NPs. We use PAI and fluorescent imaging (FI) to assess the spatial distribution of ICG/NPs in tissues.

Results—A reversible $41 \pm 12\%$ ($n = 8$) decrease in diameter of the left posterior cerebral artery (PCA) relative to the right after FUS treatment is found using CD images. The spectral unmixing of photoacoustic images of the *in vivo* (2 h post FUS), perfused, and *ex vivo* brain reveals a consistent distribution pattern of ICG and NPs at *FUS locations. *Ex vivo* spectrally unmixed photoacoustic images show that the opening width is, on average, 1.18 ± 0.12 mm and spread laterally 0.49 ± 0.05 mm which correlated well with the BBB opening locations on MR images. *In vivo* PAI confirms a deposit of NPs in tissues for hours and potentially days, is less sensitive to NPs of lower absorbance at a depth greater than 3 mm and too noisy with NPs above an

Correspondence to: Johann Le Floch¹; jlefloch@sri.utoronto.ca.

Conflict of Interest

FSF consults for and receives grant funding from Fujifilm VisualSonics Inc.

Compliance with Ethical Standards

Ethical Statement

All experimental procedures were approved by the Animal Care Committee at Sunnybrook Research Institute, University of Toronto.

Publisher's Note. Springer Nature remains neutral with regard to jurisdictional claims in published maps and institutional affiliations.

Electronic supplementary material The online version of this article (<https://doi.org/10.1007/s11307-019-01397-4>) contains supplementary material, which is available to authorized users.

absorbance of 85.4. FI correlates well with *ex vivo* PAI to a depth of 3 mm in tissues for small NPs and 4.74 mm for large NPs.

Conclusions—3DCD can monitor BBBD over time by detecting *reversible* anatomical changes in the PCA. *In vivo* 3DPAI at 15 MHz combined with circulating ICG and/or NPs with suitable properties can assess BBB opening 2 h post FUS.

Keywords

Photoacoustic; Nanostructures; Blood-brain barrier; Focused ultrasound therapy; Color Doppler; Fluorescence microscopy

Introduction

Overcoming the blood-brain barrier (BBB) non-invasively to deliver therapeutic agents to cerebral tissues has been a real challenge for years. Mannitol infusion causes the tight junctions to momentarily stretch, thus increasing the delivery of drugs into neuronal tissues; however, the entire BBB is affected, potentially leading to adverse effects [1]. Vasodilators can also increase BBB permeability by downregulating tight junction proteins [2, 3]. Intranasal administration of drugs is less invasive but offers poor absorption and an inconsistent delivery through the olfactory epithelium [4, 5]. Despite the design of nanoparticles (NPs) to target disease sites across the BBB [6–8], often only 1 % of the initial intravenous NP dose crosses the BBB [9]. Even with NPs conjugated with ligands that interact with specific receptors, only 5 % of the initial dose crosses the BBB [10]. Focused ultrasound (FUS) with circulating microbubbles was shown to create transient and reversible permeabilization of vasculature [11]. Since then, BBB disruption with FUS and microbubbles has become a therapeutic method investigated in many pre-clinical studies and is being investigated in several clinical trials ([NCT02986932](#), [NCT01827904](#), [NCT02252380](#), and [NCT01986296](#)) due to key advantages, namely, that the process is safe, reversible, non-invasive, repeatable, and more targeted than other options, thereby solving, to some extent, challenges in delivery across the BBB [12, 13].

To date, the imaging modality used to guide, verify, and monitor BBB disruption (BBBD) in clinical and pre-clinical studies has been magnetic resonance imaging (MRI) *via* gadolinium-based contrast agent enhancement (GBCA), precluding broader use of this method due to MRI cost [11, 14, 15]. Other alternative imaging methods for pre-clinical studies such as micro-CT and single-photon emission CT exist but come with important limitations. Both imply exposure to ionizing radiation that often hinders running repeated scans of the same animal required for longitudinal studies. Two-photon imaging techniques have also been used to study the effect of disruption caused by FUS; however, this technique is limited to the first millimeter in depth and often requires the opening of the skull [16, 17]. The skull optical clearing window has however recently suppressed the need of mouse craniotomy and permitted the monitoring of the disrupted BBB permeability with micrometer resolutions in the mouse cortex [18, 19]. The acoustic mapping of the cavitation signal has been successfully correlated to BBB opening and drug delivery outcomes in the non-human primates and shown potential for clinical translatability [20, 21]. Finally, photoacoustic imaging (PAI) of the BBB has previously shown promise in the rat brain but

was limited to absorbers at 800 nm and made use of a craniotomy, which limits the clinical translatability [22].

The purpose of this paper is to establish a proof of principle of the *in vivo* PAI and 3D color Doppler (3DCD) ability to detect FUS-induced BBB openings in mice. In particular, we report on the use of 3DCD ultrasound to assess, over three time points, physiological and anatomical changes due to the application of FUS. Further, we show that *in vivo* and *ex vivo* multifrequency PAI is capable of (1) reporting the activity of custom photoacoustic contrast agents over a wide range of near infrared (NIR) wavelengths, (2) detecting their diffusion into neural tissue after FUS-mediated BBBD, and (3) studying the spatial distribution of small, medium, and large NPs at FUS locations.

Material and Methods

Preparation of Multiple Components of Nanoparticles

NPs were prepared using the flash nanoprecipitation (FNP) method as detailed in Electronic Supplementary Material (ESM) (Fig. 1a) [23]. Some NPs were tagged with a fluorophore, and, in particular, NPs of three different diameters were labeled with three different fluorophores (Alexa-488, Alexa-405, and Alexa-647, Sigma, USA) using FNP allowing for *in vivo* PAI and *ex vivo* fluorescent imaging (FI) investigations in the same animal as described in “PAI” and “FI”. The NP optical properties used in this study are reported in Table 1.

Experimental Imaging Protocol

All experimental procedures were approved by the Animal Care Committee at Sunnybrook Research Institute, University of Toronto.

Ultrasound-Mediated BBBD

MRI was performed to localize brain anatomical areas for treatment with FUS and confirm, post treatment, the creation of four openings separated by 1.4 mm in the left hemisphere (LH) of healthy CD1 mice (Charles River Laboratory, 4–6 weeks of age, $n = 8$) as described in detail in ESM.

3DCD and PAI

The assessment of BBB and the NP distribution pattern was investigated using the 3DCD and 3D photoacoustic modes of a commercial system (Vevo LAZR, FUJIFILM VisualSonics Inc., Toronto, Canada) equipped with a 15-MHz photoacoustic probe [24]. For *in vivo* PAI, the probe was fitted with a 10×2 mm external bifurcated narrow fiber bundle and was used for *in vivo* PAI and ultrasound (US) imaging of live animals (Fig. 1c). For *ex vivo* experiments, a 40-MHz probe was used. Further experimental details are found in ESM.

FI from Histology

To confirm the presence or absence of NPs in neuronal tissues, brain slices were obtained at *FUS locations and assessed by FI as detailed in ESM.

Imaging Time Frame

In Fig. S1, the experimental procedures and timeline of the protocol are summarized and further detailed in ESM.

Data Analysis

MR images were reconstructed using a custom-built script in MATLAB (USA). All photoacoustic images were processed post acquisition using the Vevo LAZR software (Fujifilm VisualSonics Inc., Toronto, Canada). The diameters of the left and right posterior cerebral arteries (LPCA, RPCA) were measured on six consecutive image slices from the *in vivo* 3DCD images and averaged. The spectrally unmixed photoacoustic images (SUPAI) were calculated using implemented algorithms [25]. For the study of the spatial distribution of NP784–40 (40 nm in diameter), NP774–240 (240 nm in diameter), and NP867–100 (100 nm in diameter) at *FUS locations, the injected dose of each NP in an individual mouse was calculated so that absorbance or dyes' concentration was similar (Table S1). Further details are in the ESM.

Results

Transcranial Monitoring with 3DCD Imaging

The detection of major brain vessels with CD was successfully achieved ($n = 8$). A significant ($p < 0.0001$) decrease in diameter of LPCA relative to RPCA on the reconstructed 3DCD rendering was consistently observed (Fig. 2). At baseline, LPCA and RPCA were, on average, $1.01 \text{ mm} \pm 0.06 \text{ mm}$ and $1.04 \text{ mm} \pm 0.04 \text{ mm}$ in diameter, respectively, and were found statistically not different ($p = 0.28$). In contrast and 2 h following FUS, LPCA and RPCA were, on average, $0.58 \text{ mm} \pm 0.02 \text{ mm}$ and $0.98 \text{ mm} \pm 0.04 \text{ mm}$ in diameter, respectively (reported as mean \pm SEM and calculated from measurements reported in Table 2) and were found statistically different ($p < 0.0001$). Likewise, RPCA measurements at baseline compared with those of RPCA 2 h following FUS were found not statistically different ($p = 0.09$). At 4 days, LPCA and RPCA were, on average, $0.85 \text{ mm} \pm 0.01 \text{ mm}$ and $1.14 \text{ mm} \pm 0.03 \text{ mm}$ in diameter, respectively, and therefore closer to their baseline values. The observed CD blood velocities measured in LPCA were consistently smaller relative to those observed in RPCA, 2 h following FUS (Fig. 2b and Fig. S2b). Four days post FUS, LPCAs almost reached their diameter baseline values (Fig. 2c, Fig. S1c, and Table 2). Also, the calculated difference in diameter between RPCA and LPCA relative to RPCA was, on average, $11 \% \pm 4 \%$, $41 \% \pm 12 \%$ ($p < 0.0001$), and $25 \% \pm 3 \%$ at baseline, 2 h, and 4 days post FUS, respectively (Fig. 2d).

PAI

NPs with three different diameters display sharp and well-separated spectral peaks at 700, 785, and 875 nm, respectively (Fig. S3). The ICG spectrum exhibited a broad peak at approximately 810 nm.

In Vivo Detection of BBB with PAI

In vivo, no increase in photoacoustic signal intensities (PASI) was observed with the tested 10-mg/kg concentration of ICG, even though FUS with microbubbles successfully created 4 openings in this animal as confirmed by MRI. However, stronger PASI in brain tissues relative to baseline in both hemispheres, 2 h post FUS following ICG injection (30 and 50 mg/kg), were observed consistently *in vivo* ($n = 4$) with a return to baseline PASI in both hemispheres 4 days post FUS ($n = 1$) (Fig. 3a). In addition, the profile along the scanning direction of the averaged PASI of LH exhibited 4 peaks indicating the 4 openings created by FUS. In contrast, the baseline profiles of LH and RH did not exhibit any substantial differences (Fig. 3).

Likewise, consistent unilateral and strong PASI were observed *in vivo*, in LH at wavelengths specific to the photoacoustic contrast agents, confirming the presence of NPs ($n = 6$) and ICG ($n = 4$) where the BBB was disrupted (Fig. 4a). Although the boundary of the BBB opening was more difficult to delineate *in vivo* (Fig. 5a–c “skin intact”), mainly due to the attenuation of the US signal caused by the skull, our findings indicated that the skin and/or the skull did not adversely impact the variations in PASI of the NPs/ICG between LH and RH at most locations, with peaks correlating to a BBB opening separated by about 1.4 mm in the scanning direction.

Spatial Distribution of NPs Versus ICG at BBB Locations

The unilateral presence and diffusion of NPs was further demonstrated with the 3D rendering of the *ex vivo* mouse brain showing strong PASI at the FUS openings at each wavelength, corresponding to the peak of each dye's spectrum (Fig. 6). The openings were very similar to those confirmed by MRI immediately following FUS, as indicated by MR signal enhancement due to the leakage of GBCA into brain tissues.

Ex vivo photoacoustic coronal images (excised brain following cardiac perfusion) at specific wavelengths showed NP867–100 deposits within brain tissues to a maximum distance of 4.64 mm with an average of 2.26 ± 0.20 mm. The corresponding lateral spread was 0.49 ± 0.05 mm ($n = 5$) with a maximum of 0.68 mm. The BBB opening width in the scanning direction was found to be 1.18 ± 0.12 mm. The maximum depth at which NPs were detected was 4.74 mm into brain tissues (NP867–100 and NP774–240). Furthermore, NP867–100 remained active in neuronal tissues in perfused and excised tissues whereas ICG, which washed out more markedly in deep brain tissues following cardiac perfusion, was only detected within the first mm (Fig. 4b, c “perfused”).

Effect of Size, Dye Concentration, and Maximum Absorbance on NP Pattern Distribution

Interestingly, NP784–40 and NP867–100 showed marked variations in terms of spatial diffusion into brain tissues in *in vivo* and *ex vivo* photoacoustic images (Fig. 4c). In Fig. 5, MRI showing the 4 openings created by FUS is compared to the 3D rendering of photoacoustic images of the whole *ex vivo* brain. The spectrally unmixed PASI indicated a more pronounced spatial extent of NP867–100 and NP774–240 than NP784–40, throughout all BBB openings. The NPs were delivered at the same dye concentration in mouse total blood volume, but the former two NPs are both larger in size (2.5 and 6 times greater,

respectively) and have greater maximum absorbance (5 and 6.3 times greater, respectively). NP784–40 accumulated preferentially in two of the 4 openings (regions 2 and 3), and its spatial distribution did not seem to expand beyond the location of FUS treatment as much as the other two populations of NPs (Fig. 5f–h and Fig. S6). NP867–100 and NP774–240 diffused into brain tissues more broadly than the smaller NPs at most and around BBB openings (Fig. S6). This change in pattern distribution was also consistently observed within the first 3 mm in brain tissues on *ex vivo* SUPAI normalized for maximum absorbance (Fig. S7).

While the greater peak absorbance of NP774–240 makes these nanoparticles unsuitable for *in vivo* PAI because of the resulting strong PASI saturating the image (Fig. 6a), they were observed, as opposed to other NPs, in all brain regions where enhanced permeability was also found on T1-w MRI following FUS (Fig. 6a, e and Fig. S6).

FI

None of the tagged NPs exhibited any fluorescent signals in RH at locations where FUS was not applied. In contrast, there was a consistent fluorescent signal from all NPs in LH at *FUS locations (Fig. 6d and Fig. S5e). The spatial extent observed correlated overall well with *ex vivo* photoacoustic images for each of the tagged NP (Fig. 6c, d) as did the histology showing the spatial extent of Alexa-488-NP867–100 (Fig. S5c–e). However, strong fluorescent signals were consistently observed at the brain base (Fig. 6d) whereas rather low or no PASI were observed at this depth depending on the type of NPs and US frequencies used (Fig. 6b, c).

Discussion

This study is the first to report the BBBD detection in 3D through intact mouse skull using PAI combined with FUS-mediated ICG/NPs delivery. Additionally 3DCD permits the monitoring of the reversible changes in PCA associated with BBBD. We also show sustained simultaneous accumulation, *in vivo across the BBB*, of three sizes of fluorophore-labeled NPs.

Detected Anatomical and Physiological Changes of Major Blood Vessels

The significant 41 % decrease in LPCA diameter, 2 h post FUS, is probably due to the microbubbles interaction with brain tissues at the time of sonication. Likewise, the change in blood flow velocities is likely explained by the alterations of PCA morphology at the time of sonication. As expected [26], the changes observed 4 days post FUS in LPCA using 3DCD confirm that the BBB opening is reversible.

Regarding the measured blood vessel diameter, it is based on a constant predetermined threshold and is an overestimation. However, as long as the geometry and US scanner settings are kept identical, the observed relative changes are meaningful and the calculated blood velocities reflect also real changes in flow.

BBB Detection with PAI and Spatial Distribution of Multiple Components of NPs

At *FUS locations, the 3D rendering of the *ex vivo* mouse brain showed a unilateral and strong PASI at wavelengths corresponding to the peak of each dye's spectrum (except for the lowest concentration of ICG tested, most probably because the PASI was too weak to be detected). The perfused and *ex vivo* coronal view further characterized the BBB openings demonstrating the presence of NPs over a range of depths in neuronal tissues. The opening of BBB by FUS seemed to benefit more the NPs than ICG in terms of depth penetration into tissues at the studied time points. Once in the vasculature, ICG is bound to plasma proteins, in particular about 80 % to globulins (ICG-G) and about 20 % to albumin (ICG-A). Hence, both molecules were responsible for the PASI observed in the vasculature with ICG-G likely contributing the most to the PASI *in vivo*. In addition, presumably only a small concentration of ICG-A accumulated into brain tissues within the first 2 h after FUS treatment since (1) only high concentrations of tested ICG were detected *in vivo*, (2) SUPAI of the perfused brain showed the presence of ICG mainly at the surface of the BBB opening, and (3) ICG-G is much larger than ICG-A and would therefore likely not cross the BBB opening as indicated elsewhere [27]. Thus, both ICG-A and NPs diffused into the brain tissue upon US irradiation as observed *in vivo* and *ex vivo* 2 h post FUS. At later times, NPs were retained in the tissue, do not diffuse back into the bloodstream, and were visible *in vivo* in the brain 4 days post FUS.

Although PAI alone at these high frequencies does not offer a sufficient contrast to guide FUS *in vivo* as the skull distorts and attenuates the US echoes from brain structures, lower frequencies may be more suitable for this purpose [28]. Nevertheless, this would be at the cost of much reduced spatial resolution, and thus, the design and construction of a dedicated high-frequency photoacoustic transducer for mouse brain imaging may be desirable. In addition, the development of algorithms to correct for the skull could improve the quality of the *in vivo* PAI. Notably, *in vivo* PAI at these high frequencies combined with NPs demonstrated a clear increase in PASI at *FUS locations as long as the absorbance of NPs was lower than 85.

It was found that NPs with different properties, *i.e.*, size, dye concentration, NP concentration, and absorbance of NPs, seemed to play a role in the way NPs spread laterally into neuronal tissues. The difference in spatial distribution of these three NPs formulations observed *in vivo*, within the width of the BBBD (*z* direction) and within the first 3 mm in depth from the surface of the brain (*x* direction), and confirmed with 3D *ex vivo* PAI and FI, was consistent with the same dye concentration and maximum absorbance and suggests that attenuation of PASI alone could not be responsible for these variations and that a change in diameter might be responsible for the spatial distribution. However, the discrepancies between *ex vivo* and *in vivo* photoacoustic images normalized for dye concentration, in terms of the presence of NPs deeper into brain tissues (deeper than 3 mm from the surface of the brain) as observed in SUPAI *in vivo*, is likely due to tissue attenuation. For the photoacoustic images of *ex vivo* excised brains normalized for dye concentration, higher-frequency components are detected by the 40-MHz transducer, so the higher-frequency PASI from deeper tissue may be attenuated to below detection levels. Further investigations would

be required to explain the specific role of size, absorbance, and the microenvironment in determining the pattern distribution of the three NPs.

It is worth noting that 3D *ex vivo* PAI combined with NPs with strong maximum absorbance (> 85) and FI findings correlated well with any apparent discrepancy, observed at the base of the brain *in vivo*, most probably due to the lack of light delivery at that depth at the NP784–40-specific wavelength and due to US attenuation at 40 MHz *ex vivo* (Fig. 6c). Therefore, 3D *ex vivo* PAI with suitable NP properties could potentially provide complimentary 3D information on the spatial progression of brain diseases without destructively slicing the brain.

Advantages of Custom-Made NPs

These NPs have several advantages over nanosized particles. Gold nanorods required chemical synthesis into 3D structures with sizes that can vary resulting in variation in photoacoustic contrast [29–32]. Carbon nanotubes suffer from broad absorbance spectra profiles, hence limiting the ability to multiplex in the NIR range [33–35]. Liposomes have loadings of hydrophobic dyes that are limited to the surface of the particle or within the lipid bilayer, resulting in loadings generally below 5 % *w/w* [36–39]. In contrast, these NPs utilize molecular dyes that are identical from each batch, have sharp absorbance peaks permitting multiplexed PAI, have dye loadings > 50 % *w/w*, or can also be dual photoacoustic-PET imaging active [23, 40, 41]. Thanks to their long circulation time [42, 43], these NPs could potentially access the extravascular space and target cells more efficiently.

Conclusion

3DCD US can monitor BBBB by FUS and suggested that physiological and anatomical changes occurred within the first 2 h following FUS, and thereafter, a return towards baseline was likely initiated. BBBB by FUS allows the deposition of NPs and ICG at concentrations equal to and above 30 mg/kg into mouse brain tissues. PAI combined with absorbance below 85 and 100 nm NPs and 240 nm NPs can detect *in vivo* BBBB. Forty-nanometer NPs were difficult to detect *in vivo* with PAI due to their low absorbance, despite also penetrating neuronal tissues. Therefore, 40 nm NPs appear less suitable as potential theranostic agents in brain PAI applications.

FUS locations = locations where FUS was applied.

Supplementary Material

Refer to Web version on PubMed Central for supplementary material.

Acknowledgments

We would like to acknowledge Yin, Rideout-Gros, and Nghiem for their help with animal care, So for histology, Mikloska and Seerala for MRI, and FUS and Heinmiller for PAI.

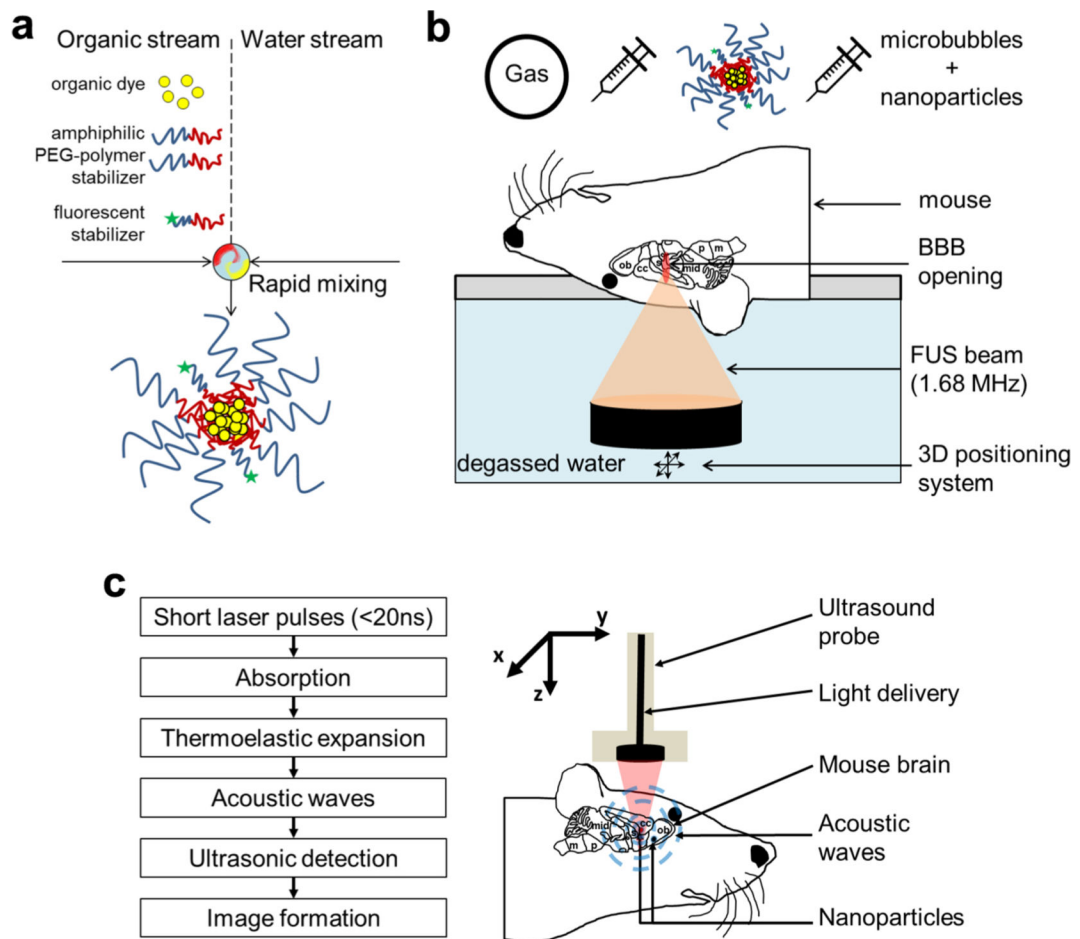
Funding Information. JLF and FSF were funded by TFRI under grant number 1022 and CIHR grant FDN148367. RKP was funded by Princeton SEAS Blaire/Pyne and Old Guard. KH was funded by NIH under grant number R01-EB003268 and CRC.

References

1. Gonzales-Portillo GS, Sanberg PR, Franzblau M, Gonzales-Portillo C, Diamandis T, Staples M, Sanberg CD, Borlongan CV (2014) Mannitol-enhanced delivery of stem cells and their growth factors across the blood-brain barrier. *Cell Transplant* 23:531–539 [PubMed: 24480552]
2. Lee HJ, Zhang Y, Pardridge WM (2002) Blood-brain barrier disruption following the internal carotid arterial perfusion of alkyl glycerols. *J Drug Target* 10:463–467 [PubMed: 12575736]
3. Black KL, Cloughesy T, Huang S-C, Gobin YP, Zhou Y, Grous J, Nelson G, Farahani K, Hoh CK, Phelps M (1997) Intracarotid infusion of RMP-7, a bradykinin analog, and transport of gallium-68 ethylenediamine tetraacetic acid into human gliomas. *J Neurosurg* 86:603–609 [PubMed: 9120622]
4. Costantino HR, Illum L, Brandt G, Johnson PH, Quay SC (2007) Intranasal delivery: physicochemical and therapeutic aspects. *Int J Pharm* 337:1–24 [PubMed: 17475423]
5. Lochhead JJ, Thorne RG (2012) Intranasal delivery of biologics to the central nervous system. *Adv Drug Deliv Rev* 64:614–628 [PubMed: 22119441]
6. Goldsmith M, Abramovitz L, Peer D (2014) Precision nanomedicine in neurodegenerative diseases. *ACS Nano* 8:1958–1965 [PubMed: 24660817]
7. Patel T, Zhou J, Piepmeier JM, Saltzman WM (2012) Polymeric nanoparticles for drug delivery to the central nervous system. *Adv Drug Deliv Rev* 64:701–705 [PubMed: 22210134]
8. Kreuter J (2014) Drug delivery to the central nervous system by polymeric nanoparticles: what do we know? *Adv Drug Deliv Rev* 71:2–14 [PubMed: 23981489]
9. Stockwell J, Abdi N, Lu X, Maheshwari O, Taghibiglou C (2014) Novel central nervous system drug delivery systems. *Chem Biol Drug Des* 83:507–520 [PubMed: 24325540]
10. Saraiva C, Praça C, Ferreira R, Santos T, Ferreira L, Bernardino L (2016) Nanoparticle-mediated brain drug delivery: overcoming blood-brain barrier to treat neurodegenerative diseases. *J Control Release* 235:34–47 [PubMed: 27208862]
11. Hynynen K, McDannold N, Vykhodtseva N, Jolesz FA (2001) Noninvasive MR imaging-guided focal opening of the blood-brain barrier in rabbits. *Radiology* 220:640–646 [PubMed: 11526261]
12. O'Reilly MA, Hynynen K (2012) Ultrasound enhanced drug delivery to the brain and central nervous system. *Int J Hyperth* 28:386–396
13. Miller DB, O'Callaghan JP (2017) New horizons for focused ultrasound (FUS) – therapeutic applications in neurodegenerative diseases. *Metabolism* 69:S3–S7
14. Park E-J, Zhang Y-Z, Vykhodtseva N, McDannold N (2012) Ultrasound-mediated blood-brain/blood-tumor barrier disruption improves outcomes with trastuzumab in a breast cancer brain metastasis model. *J Control Release* 163:277–284 [PubMed: 23000189]
15. Park J, Aryal M, Vykhodtseva N, Zhang YZ, McDannold N (2017) Evaluation of permeability, doxorubicin delivery, and drug retention in a rat brain tumor model after ultrasound-induced blood-tumor barrier disruption. *J Control Release* 250:77–85 [PubMed: 27742444]
16. Cho EE, Drazic J, Ganguly M, Stefanovic B, Hynynen K (2011) Two-photon fluorescence microscopy study of cerebrovascular dynamics in ultrasound-induced blood-brain barrier opening. *J Cereb Blood Flow Metab* 31:1852–1862 [PubMed: 21505473]
17. Burgess A, Nhan T, Moffatt C, Klivanov AL, Hynynen K (2014) Analysis of focused ultrasound-induced blood-brain barrier permeability in a mouse model of Alzheimer's disease using two-photon microscopy. *J Control Release* 192:243–248 [PubMed: 25107692]
18. Zhao Y-J, Yu T-T, Zhang C, Li Z, Luo QM, Xu TH, Zhu D (2018) Skull optical clearing window for in vivo imaging of the mouse cortex at synaptic resolution. *Light Sci Appl* 7:17153 [PubMed: 30839532]
19. Feng W, Zhang C, Yu T, et al. (2018) In vivo monitoring blood-brain barrier permeability using spectral imaging through optical clearing skull window. *J Biophotonics*

20. Wu SY, Sanchez CS, Samiotaki G, Buch A, Ferrera VP, Konofagou EE (2016) Characterizing focused-ultrasound mediated drug delivery to the heterogeneous primate brain in vivo with acoustic monitoring. *Sci Rep*. 10.1038/srep37094
21. Wu SY, Aurup C, Sanchez CS, Grondin J, Zheng W, Kamimura H, Ferrera VP, Konofagou EE (2018) Efficient blood-brain barrier opening in primates with neuronavigation-guided ultrasound and real-time acoustic mapping. *Sci Rep* 10.1038/s41598-018-25904-9
22. Wang P-H, Liu H-L, Hsu P-H, Lin CY, Chris Wang CR, Chen PY, Wei KC, Yen TC, Li ML (2012) Gold-nanorod contrast-enhanced photoacoustic micro-imaging of focused-ultrasound induced blood-brain-barrier opening in a rat model. *J Biomed Opt* 17:61222
23. Lu HD, Wilson BK, Heinmiller A, Faenza B, Hejazi S, Prud'homme RK (2016) Narrow absorption NIR wavelength organic nanoparticles enable multiplexed photoacoustic imaging. *ACS Appl Mater Interfaces* 8:14379–14388 [PubMed: 27153806]
24. Needles A, Heinmiller A, Sun J, Theodoropoulos C, Bates D, Hirson D, Yin M, Foster FS (2013) Development and initial application of a fully integrated photoacoustic micro-ultrasound system. *IEEE Trans Ultrason Ferroelectr Freq Control* 60:888–897 [PubMed: 23661123]
25. Luke GP, Nam SY, Emelianov SY (2013) Optical wavelength selection for improved spectroscopic photoacoustic imaging. *Photoacoustics* 1:36–42 [PubMed: 25302148]
26. Hynynen K, McDannold N, Sheikov NA, Jolesz FA, Vykhodtseva N (2005) Local and reversible blood–brain barrier disruption by noninvasive focused ultrasound at frequencies suitable for trans-skull sonications. *Neuroimage* 24:12–20 [PubMed: 15588592]
27. Lee S, Lim W, Ryu HW, Jo D, Min JJ, Kim HS, Hyun H (2017) ZW800–1 for assessment of blood-brain barrier disruption in a photothrombotic stroke model. *Int J Med Sci* 14:1430–1435 [PubMed: 29200957]
28. Razansky D, Buehler A, Ntziachristos V (2011) Volumetric real-time multispectral optoacoustic tomography of biomarkers. *Nat Protoc* 6:1121–1129 [PubMed: 21738125]
29. Kim C, Cho EC, Chen J, Song KH, Au L, Favazza C, Zhang Q, Cobley CM, Gao F, Xia Y, Wang LV (2010) In vivo molecular photoacoustic tomography of melanomas targeted by bioconjugated gold nanocages. *ACS Nano* 4:4559–4564 [PubMed: 20731439]
30. Lu W, Huang Q, Ku G, Wen X, Zhou M, Guzatov D, Brecht P, Su R, Oraevsky A, Wang LV, Li C (2010) Photoacoustic imaging of living mouse brain vasculature using hollow gold nanospheres. *Biomaterials* 31:2617–2626 [PubMed: 20036000]
31. Pan D, Pramanik M, Senpan A, Allen JS, Zhang H, Wickline SA, Wang LV, Lanza GM (2011) Molecular photoacoustic imaging of angiogenesis with integrin-targeted gold nanobeacons. *FASEB J* 25:875–882 [PubMed: 21097518]
32. Chen Y-S, Frey W, Kim S, Homan K, Kruizinga P, Sokolov K, Emelianov S (2010) Enhanced thermal stability of silica-coated gold nanorods for photoacoustic imaging and image-guided therapy. *Opt Express* 18:8867 [PubMed: 20588732]
33. Pansare VJ, Hejazi S, Faenza WJ, Prud'Homme RK (2012) Review of long-wavelength optical and NIR imaging materials: contrast agents, fluorophores, and multifunctional nano carriers. *Chem Mater* 24:812–827 [PubMed: 22919122]
34. De la Zerda A, Zavaleta C, Keren S et al. (2008) Carbon nanotubes as photoacoustic molecular imaging agents in living mice. *Nat Nanotechnol* 3:557–562 [PubMed: 18772918]
35. Mallidi S, Larson T, Tam J, Joshi PP, Karpiouk A, Sokolov K, Emelianov S (2009) Multiwavelength photoacoustic imaging and plasmon resonance coupling of gold nanoparticles for selective detection of cancer. *Nano Lett* 9:2825–2831 [PubMed: 19572747]
36. Beziere N, Lozano N, Nunes A, Salichs J, Queiros D, Kostarelos K, Ntziachristos V (2015) Dynamic imaging of PEGylated indocyanine green (ICG) liposomes within the tumor microenvironment using multi-spectral optoacoustic tomography (MSOT). *Biomaterials* 37:415–424 [PubMed: 25453969]
37. Proulx ST, Luciani P, Derzsi S, Rinderknecht M, Mumprecht V, Leroux JC, Detmar M (2010) Quantitative imaging of lymphatic function with liposomal indocyanine green. *Cancer Res* 70:7053–7062 [PubMed: 20823159]

38. Jeong HS, Lee CM, Cheong SJ, Kim EM, Hwang H, Na KS, Lim ST, Sohn MH, Jeong HJ (2013) The effect of mannosylation of liposome-encapsulated indocyanine green on imaging of sentinel lymph node. *J Liposome Res* 23:291–297 [PubMed: 23738810]
39. Cook JR, Frey W, Emelianov S (2013) Quantitative photoacoustic imaging of nanoparticles in cells and tissues. *ACS Nano* 7:1272–1280 [PubMed: 23312348]
40. Lu HD, Lim TL, Javitt S, Heinmiller A, Prud'homme RK (2017) Assembly of macrocycle dye derivatives into particles for fluorescence and photoacoustic applications. *ACS Comb Sci* 19:397–406 [PubMed: 28441473]
41. Lu HD, Wilson BK, Lim TL, Heinmiller A, Prud'homme RK (2017) Real-time and multiplexed photoacoustic imaging of internally normalized mixed-targeted nanoparticles. *ACS Biomater Sci Eng* 3:443–451
42. D'Addio SM, Saad W, Ansell SM et al. (2012) Effects of block copolymer properties on nanocarrier protection from in vivo clearance. *J Control Release* 162:208–217. 10.1016/j.jconrel.2012.06.020 [PubMed: 22732478]
43. Tang C, Edelstein J, Mikitsh JL, Xiao E, Hemphill AH, Pagels R, Chacko AM, Prud'homme R (2016) Biodistribution and fate of core-labeled¹²⁵I polymeric nanocarriers prepared by Flash NanoPrecipitation (FNP). *J Mater Chem B* 4:2428–2434. 10.1039/c5tb02172c [PubMed: 27073688]

**Fig. 1.**

FNP processes, FUS combined with nanoparticle and schematic illustration of PAI in brain tissue. **a** FNP assembly of photoacoustic nanoparticles. **b** FUS system combined with circulating microbubbles allows BBB opening. **c** PAI consists of short laser pulses absorbed locally in tissue resulting in an increase in temperature leading to a thermoelastic expansion that creates acoustic waves detectable by US. Blood and NPs are strong absorbers in NIR laser wavelengths (680 nm to 970 nm) used; therefore, the vasculature or NPs within the tissue is observed. ob: olfactory bulb; cc: cerebral cortex; s: septum; mid: midbrain; p: pons and m: medulla.

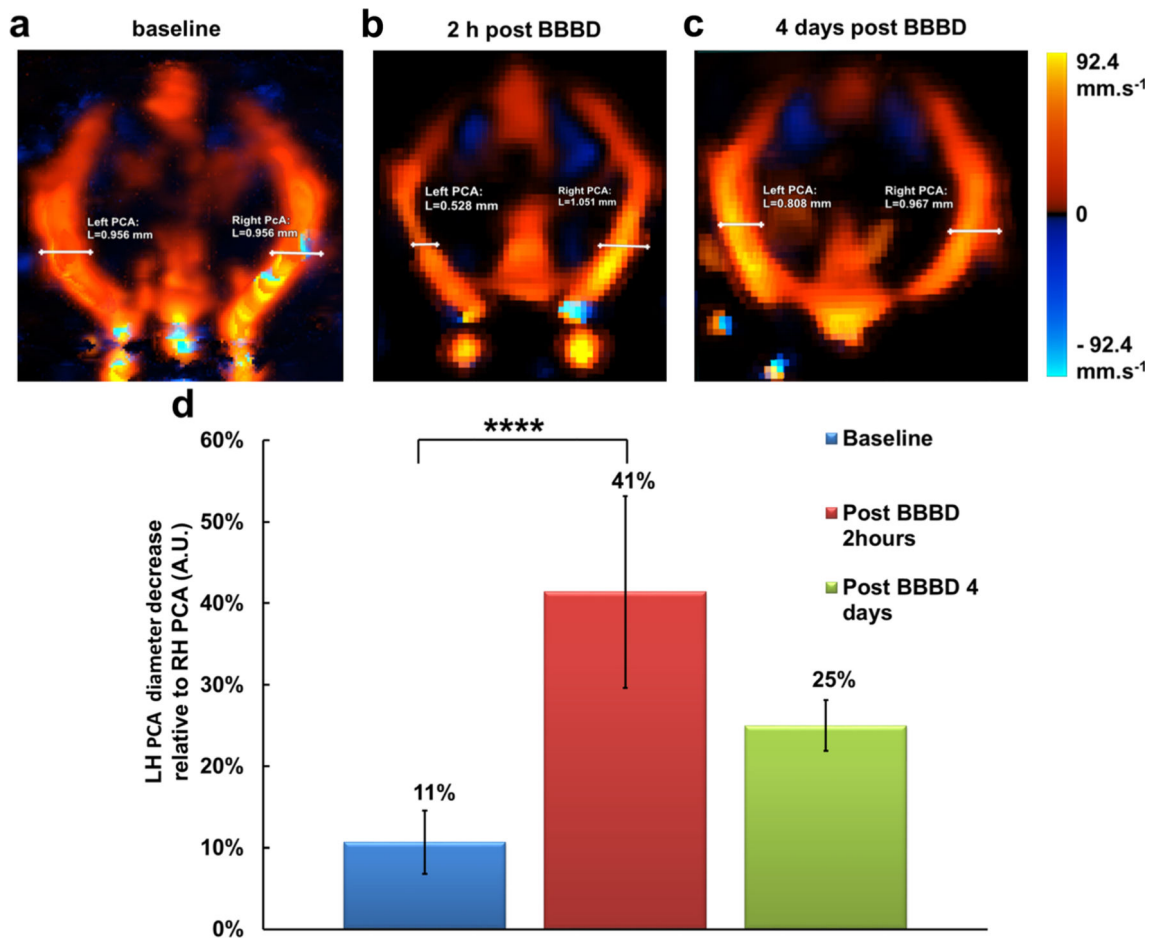


Fig. 2. 3DCD mouse brain images at **a** baseline, **b** 2 h following FUS and the injection of dyes, and **c** 4 days post FUS and the injection of dyes. Note the decrease in diameter of LH PCA 2 h following FUS. **d** Relative changes in diameter of LH PCA relative to RH PCA at studied time points (**** $p < 0.0001$).

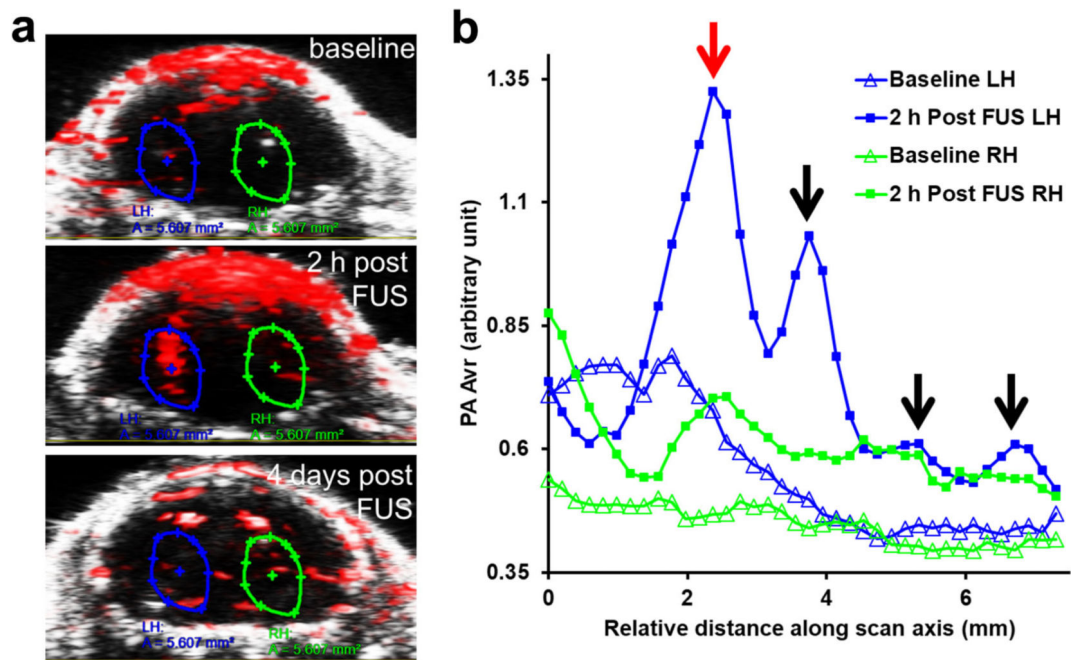


Fig. 3.

In vivo photoacoustic images and spatial profiles along the scanning direction of the mean PASI of LH and RH before and after FUS. **a** *In vivo* photoacoustic images at the ICG's spectrum maximum demonstrate on average a stronger LH (area outlined in blue) than RH (area outlined in green) PASI 2 h post FUS following ICG (50 mg/kg) injection relative to baseline PASI in both hemispheres. Four days post FUS, PASI are back to baseline PASI level. **b** The profiles correspond to *in vivo* PAI at baseline and 2 h post FUS (LH and RH profiles in blue and green, respectively). Arrows indicate the location of the 4 BBB openings. Red arrow corresponds to the *in vivo* photoacoustic image cross section location 2 h post FUS (a—middle).

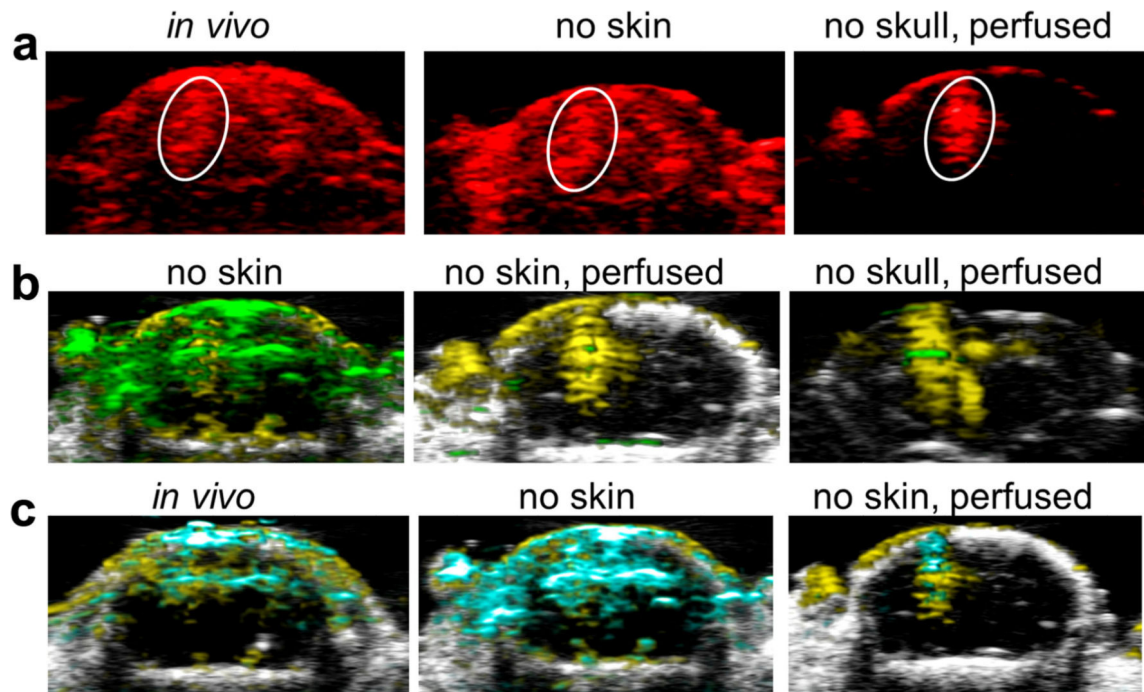


Fig. 4. *In vivo* and *ex vivo* perfused photoacoustic images with intact and removed skin and skull within 2 h post FUS. **a** Persisting stronger PASI at the dye's spectrum maximum was observed in LH, relatively to RH, *in vivo* with or without skin and skull at BBBD locations. **b** SUPAI showing ICG (green) and NP867–100 (gold) spatial extent. **c** NP867–100 (gold) and NP784–60 (light blue) spatial extent.

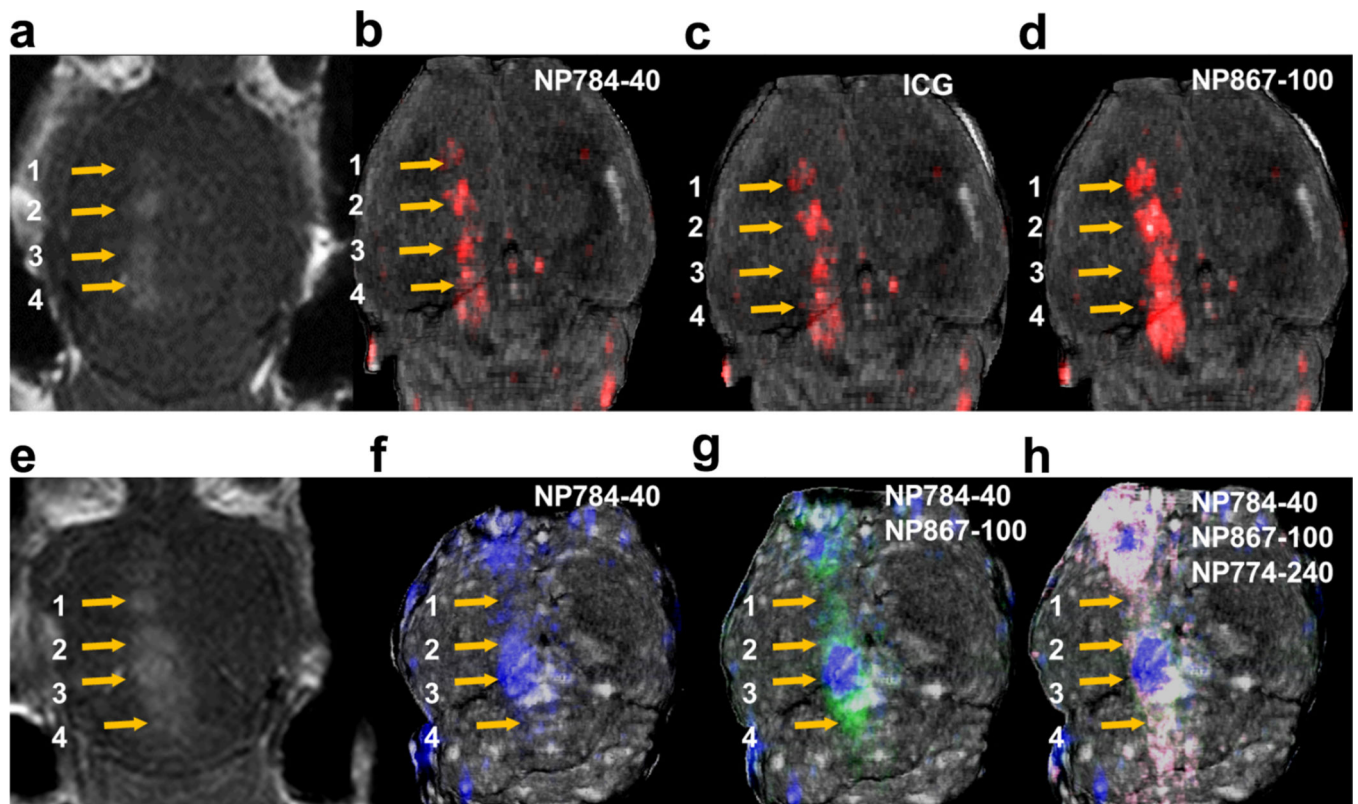


Fig. 5.
In vivo MRI and 3DPAI rendering of *ex vivo* brain 2 days following perfusion for two cases.
a, e MRI axial view of brains a few minutes after FUS treatment showed GBCA enhancement in the disrupted BBB region. Similarly, 3D renderings of the non-normalized PASI at the dye's peak wavelength of **b** NP784-40, **c** ICG, **d** NP867-100, and spectrally unmixed PASI of **f** NP784-40 (blue), **g** NP784-40 (blue) + NP867-100 (green), and **h** NP784-40 (blue) + NP867-100 (green) + NP774-240 (pink) confirmed BBB openings in these regions (arrows).

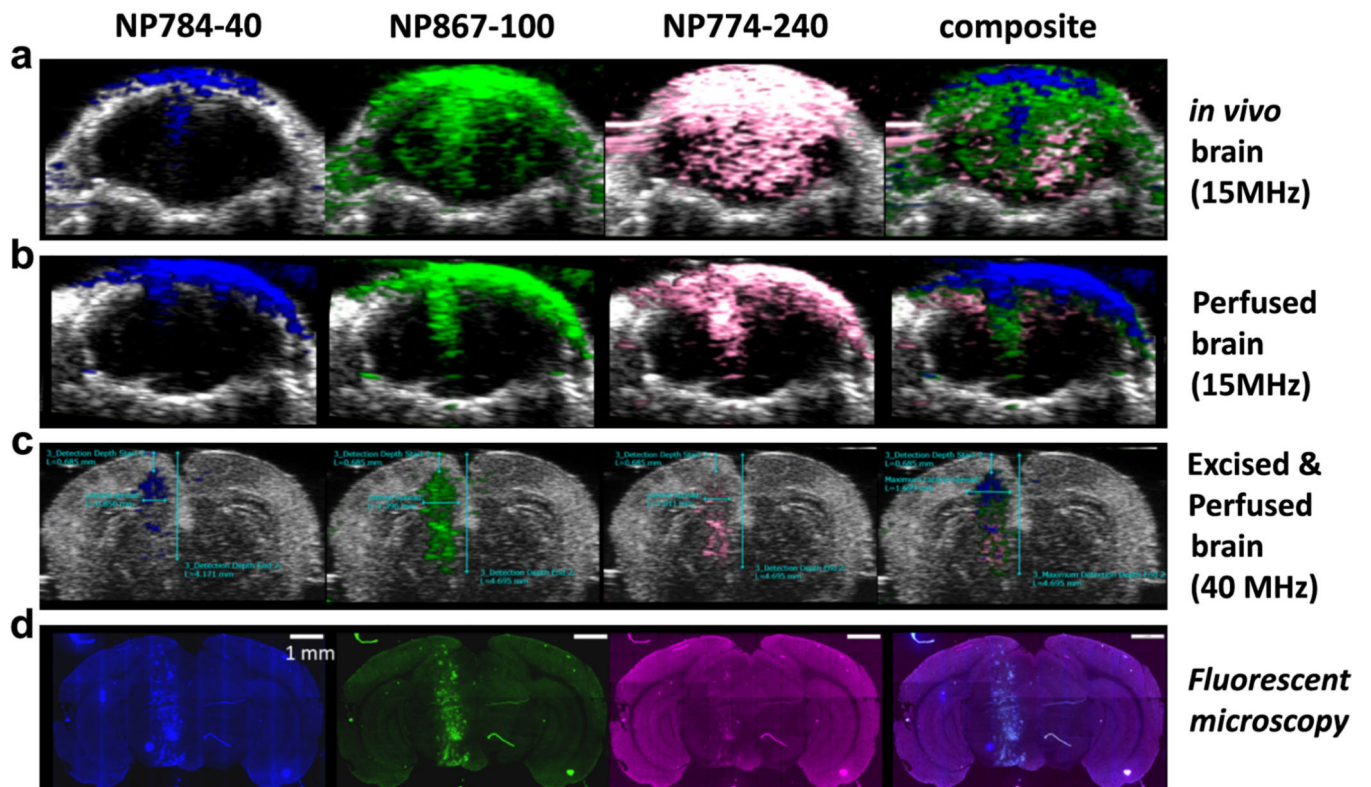


Fig. 6. SUPAI and photoacoustic images normalized for dye concentration (**a–c**) and fluorescent microscopy images (**d**) of studied NPs in the mouse brain following FUS mediated BBBB. All images are coronal view/sections located at one of the FUS BBB openings (panel **f** shown in Fig. 5). Scale bar = 1 mm. The colors in PAI correspond to the filter used in FI to detect fluorophore-labeled NPs.

Nanoparticle properties

Table 1.

Name	Diameter (nm)	Dye concentration (mg/ml)	NP concentration (mg/ml)	Abs _{max} ^a	Fluorophore
NP784-40	40-50	5	3.75	17.1	Alexa-405
NP774-240	240	15	2.55	110	Alexa-647
NP867-100	100	10	3.5	85.4	Alexa-488

^aPath length was 1 cm long and absorption measured at λ_{max} (Fig. S3)

Table 2.

PCA diameter measurements

CDI Mouse Injectate	M1		M2		M3		M4		M5		M6		M7		M8		
	Baseline	2 h	Baseline	2 h	Baseline	2 h	Baseline	2 h	Baseline	2 h	Baseline	2 h	Baseline	2 h	Baseline	2 h	
	ICG10		ICG50		NP867-100		ICG30, NP784-40, NP867-100		ICG50, NP867-100		ICG50, NP867-100		NP784-40, NP774-240, NP867-100		NP784-40, NP774-240, NP867-100		
Time points	Baseline	2 h	Baseline	2 h	4 days	Baseline	2 h	4 days	Baseline	2 h	Baseline	2 h	Baseline	2 h	Baseline	2 h	
LPCA (mm)	1.09 ± 0.13	0.64 ± 0.11	1.11 ± 0.11	0.50 ± 0.11	0.85 ± 0.18	0.88 ± 0.19	0.53 ± 0.13	0.85 ± 0.23	1.21 ± 0.09	0.50 ± 0.12	0.58 ± 0.22	0.89 ± 0.05	0.68 ± 0.06	1.26 ± 0.15	0.64 ± 0.15	0.81 ± 0.19	0.57 ± 0.08
RPCA (mm)	0.95 ± 0.08	0.96 ± 0.07	1.01 ± 0.06	1.08 ± 0.07	1.09 ± 0.10	1.03 ± 0.04	1.04 ± 0.05	1.18 ± 0.10	1.15 ± 0.03	0.73 ± 0.08	1.00 ± 0.04	0.99 ± 0.14	1.09 ± 0.14	1.29 ± 0.01	0.95 ± 0.13	1.01 ± 0.18	0.95 ± 0.05